Interaction between two unequal particles at intermediate Reynolds numbers: A pattern of horizontal oscillatory motion

Deming Nie,[1] Geng Guan,[1] and Jianzhong Lin[2,*]

[1]*Institute of Fluid Mechanics, China Jiliang University, Hangzhou, China*
[2]*State Key Laboratory of Fluid Power Transmission and Control, Zhejiang University, Hangzhou, China*

The two-dimensional lattice Boltzmann method (LBM) was used to study the motion of two interacting particles with different densities (ρ_1 and ρ_2) and diameters (d_1 and d_2), which were placed in a vertical channel under gravity. Both the density ratio ($\lambda = \rho_2/\rho_1$) and diameter ratio ($r = d_2/d_1$) between the particles were considered. The transition boundaries between the regime where the particles settle separately and the regime where the particles interact are identified by $\lambda_{\max}(r)$ and $\lambda_{\min}(r)$; they exhibit excellent power-law relationships with r. A pattern of horizontal oscillatory motion (HOM), characterized by a structure with a large (but light) particle right above a small (but heavy) one and strong oscillations of both particles in the horizontal direction, was revealed for $r \sim 0.3$ at intermediate Reynolds numbers. The results indicate that the magnitude of oscillations decreases with λ, whereas the frequency displays the opposite trend. A sudden increase in the terminal velocity of particles is seen, illustrating a transition from the classical pattern of drafting, kissing, and tumbling to the HOM at a certain λ. Upon increasing λ, the pattern of HOM may bifurcate into a vertical steady state at low Re or small r. Furthermore, the effects of the confinement ratio and particle-to-fluid density ratio were also examined. The existence of a critical confinement ratio is observed, beyond which the particles interact in a different manner.

I. INTRODUCTION

For a particulate flow, the hydrodynamic interaction between particles plays a key role in determining the flow features as well as the patterns of particle motion. In comparison with Stokes flow, the behavior of particles in nonzero Reynolds number flows becomes rich and complex due to the nonlinear effects of fluid inertia.

Owing to its academic importance, extensive efforts have been devoted to improving our understanding of the hydrodynamic interaction between particles in a particulate flow at finite Reynolds numbers. For instance, Fortes *et al.* [1] studied the sedimentation of two spheres through experiments and reported a pattern of the motion of particles known as drafting, kissing, and tumbling (DKT), through which two particles at different heights quickly exchange their vertical positions resulting from the wake effects. DKT may take place frequently for the settling of a large number of spheres, associated with the formation of clusters [2]. Recently, Dash and Lee [3] revisited the pattern of DKT at intermediate Reynolds numbers through three-dimensional simulations and experiments. They reported an inverse DKT pattern that differed from the normal pattern in the rotation direction of the turning couple during the process of tumbling. For two-dimensional analysis, Hu *et al.* [4] and Feng *et al.* [5] successively reproduced the DKT phenomenon for two circular particles through direct numerical simulations at intermediate Reynolds numbers. A similar problem was also raised by Nie *et al.* [6] and

Wang *et al.* [7], who focused on the effects of the particle arrangements and the difference in particle size on the DKT pattern, respectively. In particular, the significance of the fluid inertia on the interaction of particles was addressed by Aidun and Ding [8], who used the lattice Boltzmann method (LBM) to simulate the sedimentation of two particles under gravity in a vertical channel. They reported a variety of patterns of particle motion (i.e., periodic state, chaotic state, and periodic-doubling bifurcation) at low but finite Reynolds numbers. By extending the range of Reynolds number, Verjus *et al.* [9] revealed new features of the same sedimentation system and established a link between the terminal Reynolds number and the nondimensional driving force using a global diagram that illustrates the dynamic features of particles in a direct manner. Recently, Zhang *et al.* [10] reported two distinct symmetry-breaking phenomena for the same problem, that is, an abrupt lateral migration that gives rise to asymmetrical movement centers and a divergent oscillation that leads to an asymmetric oscillatory motion of particles with zero phase lag.

Apart from the fluid inertia, the wall effect [11–13], fluid rheology [14,15], and the presence of a large number of particles [2,16,17] may also complicate the dynamical features of a particulate flow system, which has been previously studied. In contrast, much less attention has been devoted to the case of particulate flows containing unequal particles, which has a much wider range of engineering applications. Our recent studies [18–20] indicate that, as the two-particle system is simple, the difference in the densities of particles may result in a richer but different set of dynamical features than in the case of equal particles. For the settling of two particles with different densities but the same size,

*mecjzlin@public.zju.edu.cn

our two-dimensional computations [18,19] reveal that there exist two types of periodic motion depending on the Galileo number, which have different amplitudes and frequencies with increasing density difference between particles. In particular, a discontinuous change in the settling velocity of particles is seen at a critical density difference, which is associated with a Hopf bifurcation of the particles [19]. Furthermore, numerical studies indicate that heavy particles may change their rotation sign, which results in an abrupt increase in the time period of particle oscillations [19]. In contrast, it seems likely that these discontinuous changes do not exist for a similar system in three dimensions [20]. In addition, our recent work [20] revealed that the extra dimension allows the spheres to move to the diagonal or reverse-diagonal plane of a square tube at low Galileo numbers. In particular, a quantitative comparison between the two-dimensional and three-dimensional analysis was presented in terms of the flow features, relative particle trajectory, and period of particle oscillations [20]. Despite these efforts, however, the most general case of particulate flows containing particles with different densities and sizes has not been studied. Therefore, this work aims to provide a more fundamental understanding of the interaction between two unequal particles at moderate fluid inertia. Similar to our previous work [18,19], the two-particle system was used here for which both the density and diameter ratios between particles were taken into account. For this system, a "simple" question may arise in the first place: Under what conditions do the two particles, which are subjected to the action of gravity, separate and settle individually? In other words, the first problem that should be dealt with in this work is the construction of a relationship between the particle density ratio and particle diameter ratio, which serves as a boundary for the settling of particles as a whole. The second, and of course, the most important question is how two completely different particles interact with each other in a fluid when the inertias of both fluid and particles are significant. For this, the combined effects of unequal density and size on the motion of two particles in a two-dimensional channel will be examined, and a pattern of horizontal oscillatory motion (HOM) of particles is reported.

The remainder of this paper is organized as follows. Section II briefly introduces the LBM and the treatment of moving boundaries. A description of the problem is presented in Sec. III, along with the notations used in this work. The validation procedure is presented in Sec. IV, where the DKT of two particles with different sizes but the same density is realized and compared with previous numerical results. The pattern of the HOM of particles is described in Sec. V by highlighting the effects of the Reynolds number and walls. Some concluding remarks are presented in Sec. VI.

II. METHOD

A. Lattice Boltzmann method

In this work, the motion of the fluid is solved through the single-relaxation-time LBM [21]. The discrete lattice Boltzmann equations are

$$f_i(\boldsymbol{x} + \boldsymbol{e}_i \Delta t, t + \Delta t) - f_i(\boldsymbol{x}, t) = -\frac{1}{\tau}\big[f_i(\boldsymbol{x}, t) - f_i^{(eq)}(\boldsymbol{x}, t)\big],$$

(1)

where $f_i(\boldsymbol{x}, t)$ is the distribution function for the microscopic velocity $\boldsymbol{e}_i$, and $f_i^{(eq)}(\boldsymbol{x}, t)$ denotes the corresponding equilibrium distribution function. Δt is the time step of the simulation, and τ is the relaxation time related to the fluid viscosity v. The fluid density ρ and velocity $\boldsymbol{u}$ are determined through the following formulations:

$$\rho = \sum_i f_i, \quad \rho \boldsymbol{u} = \sum_i f_i \boldsymbol{e}_i. \quad (2)$$

The popular D2Q9 (i.e., nine discrete velocities in two dimensions) lattice model was adopted here, whose discrete velocity vectors are given by

$$\mathbf{e}_i = \begin{cases} (0, 0), & \text{for } i = 0 \\ (\pm 1, 0)c, (0, \pm 1)c, & \text{for } i = 1 \text{ to } 4, \\ (\pm 1, \pm 1)c, & \text{for } i = 5 \text{ to } 8 \end{cases} \quad (3)$$

where Δx is the lattice grid, and $c = \Delta x / \Delta t$ represents the lattice speed. Following Qian *et al.* [21], the equilibrium distribution functions are chosen as

$$f_i^{(eq)}(\boldsymbol{x}, t) = w_i \rho \left[1 + \frac{3\boldsymbol{e}_i \cdot \boldsymbol{u}}{c^2} + \frac{9(\boldsymbol{e}_i \cdot \boldsymbol{u})^2}{2c^4} - \frac{3u^2}{2c^2}\right] \quad (4)$$

where w_i are the weights and $w_0 = 4/9$, w_1–$w_4 = 1/9$, and w_5–$w_8 = 1/36$. Note that for the D2Q9 model, the speed of sound has the relation $c_s^2 = c^2/3$.

By performing a Chapman-Enskog expansion, the macroscopic mass and momentum equations in the low Mach number limit can be recovered,

$$\frac{\partial \rho}{\partial t} + \boldsymbol{\nabla} \cdot (\rho \boldsymbol{u}) = 0, \quad (5)$$

$$\frac{\partial (\rho \boldsymbol{u})}{\partial t} + \boldsymbol{\nabla} \cdot (\rho \boldsymbol{u}\boldsymbol{u}) = -\boldsymbol{\nabla} p + \rho v \nabla^2 \boldsymbol{u}. \quad (6)$$

The kinematic viscosity of the fluid is determined using the equation $v = c_s^2(\tau - 0.5)\Delta t$. For the sake of simplicity, both the lattice grid and time step are fixed at 1 in this work; that is, $\Delta x = \Delta t = 1$. This is common for lattice Boltzmann simulations.

B. Boundary conditions

It is known that a special treatment for the curved boundary is usually required to ensure the no-slip boundary condition on the surfaces of solid particles immersed in a fluid. In this study, an interpolation-based bounce-back scheme [22] was employed to address this issue, which is briefly introduced below. Note that the same scheme was used in our previous studies [18–20].

Figure 1 presents a schematic of the bounce-back scheme proposed by Lallemand and Luo [22]. Note that the solid squares denote the fluid nodes located outside the curved boundary, while the solid circles denote the solid nodes that are inside the curved geometry. The open circle represents the boundary node where bouncing occurs. According to Lallemand and Luo [22], the advection (also known as "propagation") action is applied for all fluid and solid nodes after the collision process. The distribution functions that are advected from solid nodes to fluid nodes need to be recomputed

depending on the exact locations of the boundary (i.e., the boundary node). To take node A as an example, the distribution function f_7 is advected from node B. Therefore, additional computation is required to update f_7. In doing

so, a parameter q, given by $q = |AF|/|AB|$, is introduced to determine the location of boundary node F. Subsequently, an interpolation scheme is employed to recompute f_7 according to the surrounding nodes,

$$f_7(A) = \begin{cases} q(1+2q)f_5(B) + (1-4q^2)f_5(A) - q(1-2q)f_5(C) - 2w_5\rho\frac{e_5 \cdot u_w}{c_s^2} & q < \frac{1}{2} \\ \frac{1}{q(2q+1)}f_5(B) + \frac{2q-1}{q}f_7(C) - \frac{2q-1}{2q+1}f_7(D) - \frac{2w_5\rho}{q(2q+1)}\frac{e_5 \cdot u_w}{c_s^2} & q \geqslant \frac{1}{2} \end{cases}. \tag{7}$$

Here, u_w is the velocity of the moving surface at boundary node F, as illustrated in Fig. 1. Note that the simple bounce-back boundary is realized by Eq. (7) if $q = 0.5$. Readers should refer to the original paper [22] for more details.

The force and torque exerted on the solid particle by the fluid-boundary nodes are computed through a momentum exchange scheme [22,23]. In addition, to account for the effect of a solid particle entering or leaving the fluid region, the method proposed by Aidun et al. [24] is used to calculate the added force and torque due to the covered and uncovered fluid nodes. The motion of a particle is determined by solving Newton's equations using the values of net force and torque.

C. Lubrication force model

The lubrication force becomes significant when two particles come into close contact with each other. This force, generated by the attenuation of the fluid film in the gap between the two particles, is repulsive upon approach and attractive upon separation of the particles. However, when the gap between the two particles is of the order of one lattice grid, the lubrication force cannot be resolved with the LBM. To address this issue, a lubrication force model proposed by Yuan and Ball [25] was adopted in the simulations:

$$F_{\text{lub}} = \begin{cases} 0 & h > h_c \\ -\frac{3}{2}\pi\rho\nu\left(\frac{2a_1a_2}{a_1+a_2}\right)^{3/2}\left(\frac{1}{h} - \frac{1}{h_c}\right)^{3/2}(U_{12} \cdot \hat{R}_{12})\hat{R}_{12} & h < h_c \end{cases}. \tag{8}$$

Here, a_1 and a_2 are the radii of the two particles, $U_{12} = U_1 - U_2$, and $h = |R_1 - R_2| - (a_1 + a_2)$ is the distance between the particle surfaces. h_c is the cutoff distance between the particle surfaces for the added lubrication force and is fixed at $1.5\,\Delta x$ in the simulations. The unit vector is defined as follows: $\hat{R}_{12} = R_{12}/|R_{12}|$. Equation (8) can be adjusted

slightly to account for particle-wall collisions. In doing so, $U_2 = 0$ is adopted, and R_2 is the corresponding point on the wall.

III. PROBLEM DESCRIPTION

In this study, the motion of two unequal particles under gravity in an infinite two-dimensional channel was numerically investigated. As shown in Fig. 2, two circular cylinders with different diameters (d_1 and d_2) and different densities (ρ_1 and ρ_2) are released to move under gravity in a vertical channel filled with a fluid of density ρ and kinematic viscosity ν. In the simulations, we assume that $d_1 > d_2$ and $\rho_1 < \rho_2$. This study focuses on a pattern of particle behavior resulting from the interaction between the two particles.

The particle positions are designated as X (horizontal) and Y (vertical). The subscripts 1 and 2 denote the large particle and the small particle, respectively, as depicted in Fig. 2. The infinite channel is represented by a simulation box with dimensions $L \times H$. Unless otherwise stated, the width of the channel is fixed at five times the diameter of the large particle; that is, $L = 5d_1$. In addition, a moving computational domain was used to simulate an infinite channel. The upstream boundary of the computational domain is 15 d_1 upstream of the large particle, whereas the downstream boundary is 20 d_1 from it (i.e., the overall channel height is $H = 35d_1$). The normal derivative of the velocity is zero at the downstream boundary, and the velocity at the upstream boundary is zero.

Because the terminal velocity of particles cannot be predicted, the velocity scale is taken as
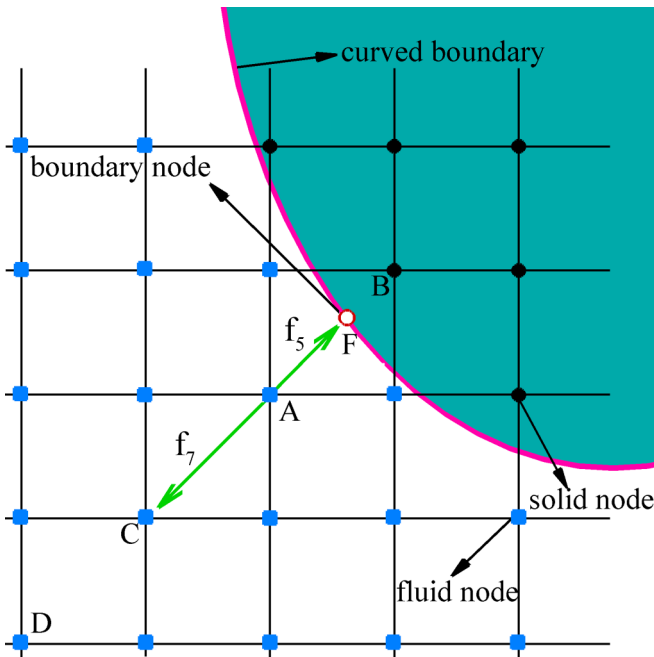
FIG. 1. Schematic of the bounce-back scheme in the LBM proposed by Lallemand and Luo [22]. Solid squares: fluid nodes; solid circles: solid nodes; open circles: boundary nodes.

$$U_0 = \sqrt{\left(\frac{\rho_1}{\rho} - 1\right)gd_1}, \tag{9}$$
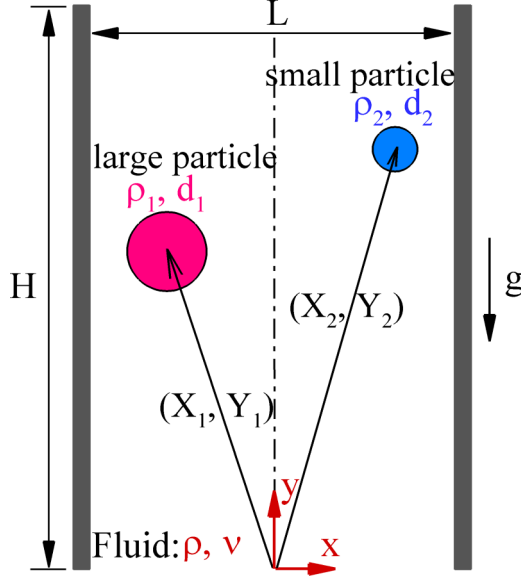
FIG. 2. Schematic of the present system and notations used in the simulations. Unless otherwise stated, the dimensions of the simulation box are fixed at $L \times H = 5d_1 \times 35d_1$, corresponding to a computational domain of 400×2800 lattice units. We assume that $d_1 > d_2$ and $\rho_1 < \rho_2$. Initially, the large particle is placed at $(-d_1, 15d_1)$ and the small particle at $(d_1, 15d_1)$.

where g is the gravitational acceleration. This reference velocity is consistent with our previous work [19,20] and other numerical studies [3]. The timescale can then be defined as $T_0 = d_1/U_0$. Moreover, the diameter of the large particle (d_1) was chosen as the length scale. This results in five dimensionless parameters that are adopted to control the present dynamical system illustrated in Fig. 2:

  Diameter ratio of the particles: $r = d_2/d_1$

  Density ratio of the particles: $\lambda = \rho_2/\rho_1$

  Density ratio of the large particle to fluid: $\gamma = \rho_1/\rho$

  Confinement ratio: $\beta = L/d_1$

  Reynolds number: $\mathrm{Re} = U_0 d_1/\nu$.

 For a better illustration, other dimensionless parameters are summarized as follows:

  Position of the large particle: $X_1^* = X_1/d_1$ and $Y_1^* = Y_1/d_1$

  Position of the small particle: $X_2^* = X_2/d_1$ and $Y_2^* = Y_2/d_1$

  Relative trajectory of the particles: $\Delta X^* = X_2^* - X_1^*$ and $\Delta Y^* = Y_2^* - Y_1^*$

  Horizontal velocity of the large particle: $U_1^* = U_1/U_0$

  Period of the particle oscillation: $T^* = T/T_0$

  Terminal settling velocity of the particles: $V_T^* = V_T/U_0$

  Minimum distance between the particles: $D_P^* = D_P/d_1$

  Minimum distance between each particle and walls: $D_{W1}^* = D_{W1}/d_1$ and $D_{W2}^* = D_{W2}/d_1$.

  Note that the definition of Re is equivalent to the Galileo number or the square root of the Archimedes number. In addition, the following parameters are fixed in the simulations unless otherwise stated: $\rho = 1$, $\gamma = 1.5$, $d_1 = 80$, and $\beta = 5$. For simplicity, these parameters are all in lattice units.

The large particle is initially placed at $(-d_1, 15d_1)$ and the small particle at $(d_1, 15d_1)$, leading to a symmetrical initial arrangement of particles, that is, $[X_1^*(0), Y_1^*(0)] = [-1, 15]$ and $[X_2^*(0), Y_2^*(0)] = [1, 15]$.

IV. VALIDATION

The present computational code has been validated through benchmark tests of particle motion in a fluid at finite Reynolds numbers in our previous studies [18,19]. To further examine the credibility of our code in dealing with the hydrodynamic interaction between particles, the DKT of two particles with different sizes but same density was reproduced and compared with the previous numerical results [7], as illustrated in Fig. 3. The selected physical parameters were the same as the ones used by Wang *et al.* [7]; i.e., $\rho = 1\,\mathrm{g\,cm^{-3}}$, $\mu = 0.01\,\mathrm{g\,cm^{-1}\,s^{-1}}$, $d_1 = 0.2\,\mathrm{cm}$, $d_2 = 0.1\,\mathrm{cm}$, and $\rho_1 = \rho_2 = 1.01\,\mathrm{g\,cm^{-3}}$. The computation was performed in a box of width $\times$ height $= 2\,\mathrm{cm} \times 18\,\mathrm{cm}$, representing a computational domain of 500×4500 lattice grids. No-slip boundary conditions were employed for all the walls. Initially, the large particle is located at $(0, 14.6\,\mathrm{cm})$ and the small particle is located at $(0, 15\,\mathrm{cm})$. Then, the particles are released from rest and begin to settle under gravity. Note that the collision strategy [26], adopted by Wang *et al.* [7], was also used in the present computation to treat the close contact between particles.

Figures 3(a) and 3(b) present the time history of the vertical positions and velocities of both particles, illustrating the well-known pattern of DKT. In comparison with the case of identical particles, however, a significant difference is clearly observed for the present case. After the process of "tumbling," the two particles depart quickly and the large particle still take the lead as a result of the larger settling velocity [Fig. 3(b)]. Therefore, the pattern of DKT occurs only once. Moreover, from Fig. 3, it can be seen that our results agree well with those reported by Wang *et al.* [7], indicating that our code is effective in dealing with the interaction between unequal particles.

It is known that the initial arrangement of particles can significantly influence the pattern of particle motion. To verify this, additional simulations were carried out using different initial particle arrangements. In doing so, the initial position of the small particle is varied while that of the large particle remains unchanged. The relative trajectories constructed by ΔX^* and ΔY^*, reflecting the relative motion of the small particle with respect to the large one, are presented in Fig. 4 for $r = 0.3$ and $\lambda = 2.12$ at $\mathrm{Re} = 50$. Five sets of initial particle arrangements were taken into account. Note that $(2, 0)$ represents the relative position of the small particle described in Sec. III. It is clearly seen that all the results achieve the same periodic solution after the initial transients die down. This suggests that the present findings hold for a variety of initial particle arrangements. In addition, Fig. 4 reveals a pattern of particle motion in which the particles are seen to oscillate horizontally when settling in the channel. This is referred to as the pattern of horizontal oscillatory motion (HOM), which will be explored in further detail in this paper.

Our previous studies [19,20] show that the collision strategy has limited influence on the motion of particles. To add
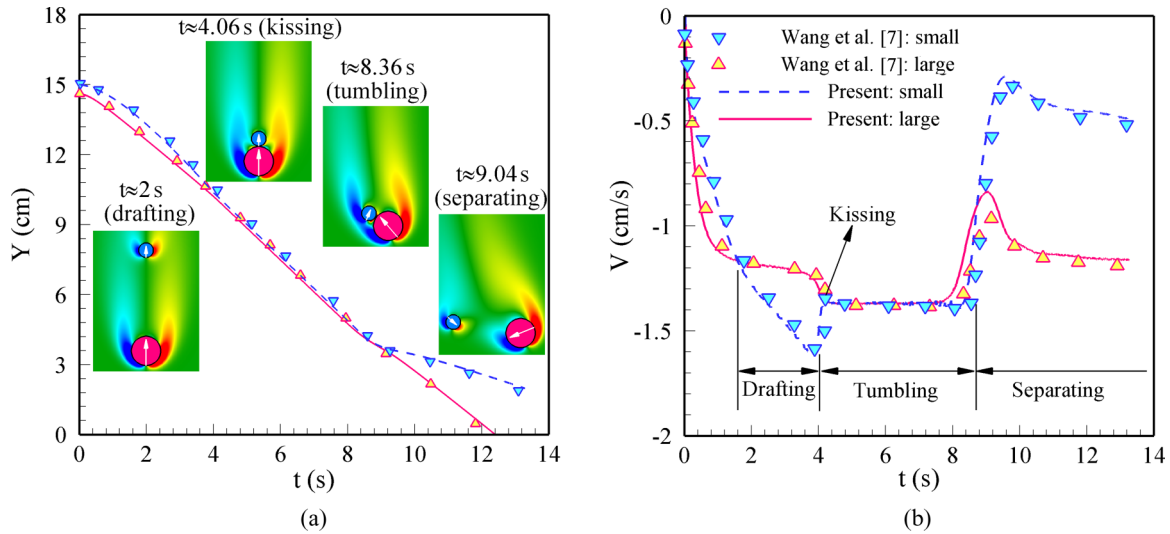
FIG. 3. Comparison with previous numerical results [7]: time history of (a) vertical positions and (b) settling velocities of both particles.

more credibility to the present results, additional simulations were carried out to provide an examination of collision models, which is illustrated in Fig. 5. For the lubrication model used here [i.e., Eq. (8)], apart from $h_c = 1.5$, another two values of h_c (i.e., $h_c = 0.5$ and 2.5) were adopted to check the effects of the cutoff distance. Little discrepancy is seen in the relative particle trajectories at the initial stage resulting from different values of h_c, as shown in Fig. 5. However, all results converge to the same periodic solution (HOM) eventually. On the other hand, the repulsive model was also used to handle the

close contact of particles in the literature. To provide a direct comparison, the repulsive models proposed by Wan and Turek [26] and Glowinski *et al.* [27] were taken into account in this section. As seen in Fig. 5, clear but limited discrepancy exists in the relative particle trajectories predicted by the lubrication model [25] with respect to those obtained by the repulsive models [26,27]. However, this discrepancy is reasonable by
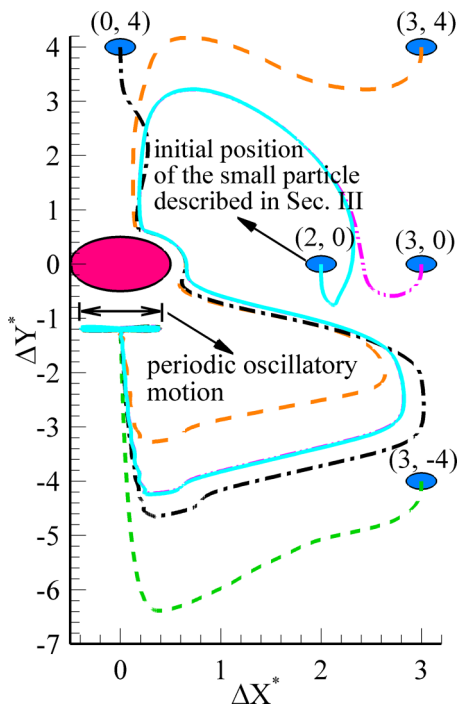
FIG. 4. Effects of the initial arrangements on the relative trajectory of the small particle with respect to the large one. Note that $\Delta X^* = X_2^* - X_1^*$ and $\Delta Y^* = Y_2^* - Y_1^*$. The parameters were chosen as $r = 0.3$, $\lambda = 2.12$, and Re $= 50$. The particles appear as ellipses because of the stretched coordinates.
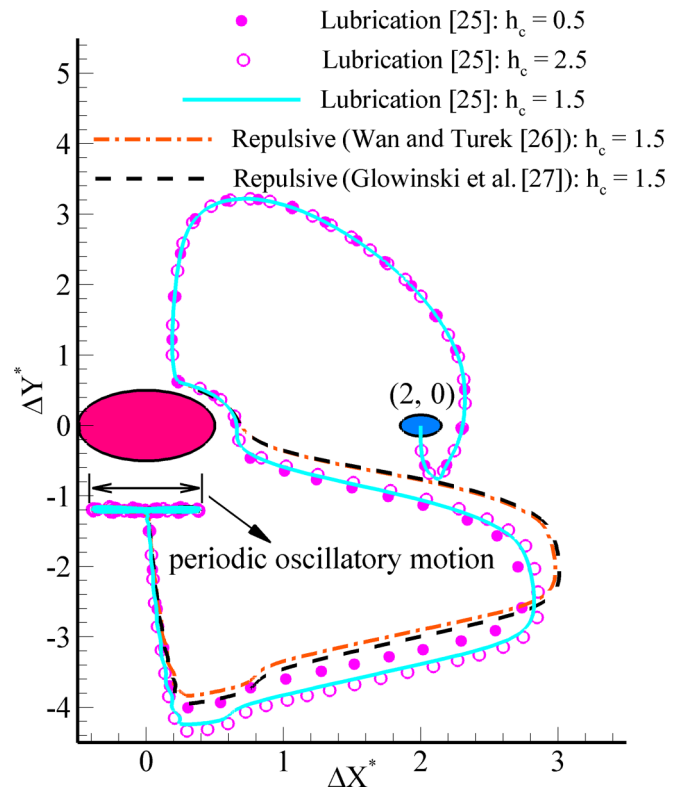
FIG. 5. Examination of the effects of collision strategy on the motion of particles. Apart from the lubrication model [25], the repulsive models proposed by Wan and Turek [26] and Glowinski *et al.* [27] were also taken into account. The parameters are the same as those in Fig. 4.
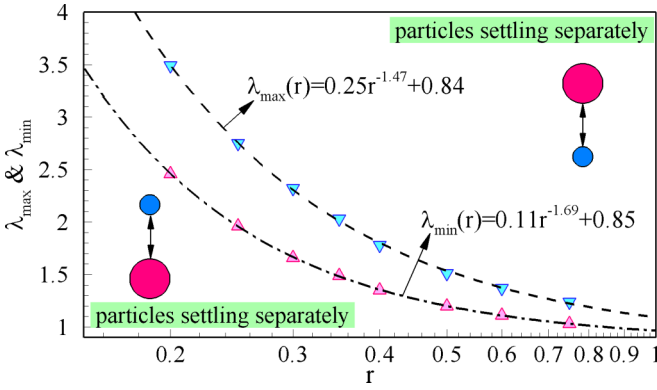
FIG. 6. Dependence of λ_{max} and λ_{min} on the diameter ratio (i.e., $r = d_2/d_1$) between particles at Re = 35. The symbols represent our simulation results, and the lines illustrate the power-law functions derived by least-square fittings (the same as below).

recalling that different collision models are originated from different mechanisms. For instance, the lubrication force [25] is repulsive upon approach while attractive upon separation of the particles. By the contrast, the repulsive force [26,27] is always repulsive. This is why the small particle is pushed farther away from the large particle right after the tumbling stage for the repulsive models (see Fig. 5). More importantly, it is seen that the same solution is reached for all models used after the initial transients die down, indicating that the choice of collision strategy does not essentially change the behavior of particles.

V. RESULTS

The interaction of two unequal particles under the action of gravity in a two-dimensional channel was numerically investigated for Reynolds numbers ranging from 10 to 50 ($10 \leqslant$ Re $\leqslant 50$) and for the diameter ratio between particles ranging from 0.2 to 0.75 ($0.2 \leqslant r \leqslant 0.75$). Most simulations were performed for a confinement ratio equal to 5 (i.e., $\beta = 5$) and a particle-to-fluid density ratio equal to 1.5 (i.e., $\gamma = 1.5$), unless otherwise stated. Note that the unequal particles settling in a fluid may separate because they have different densities and sizes. To illustrate this issue, we use λ_{max} and λ_{min} to identify the transition boundaries between the regimes where the particles settle separately and the regime where the particles interact with each other. In other words, the large particle leaves the small particle behind at $\lambda < \lambda_{min}$ and the situations flip over at $\lambda > \lambda_{max}$.

A. Overview of the motion of two unequal particles

Under what conditions will the unequal particles interact with each other all the time in the channel? This deserves our close attention. Figure 6 shows the dependence of λ_{max} and λ_{min} on the diameter ratio between particles at Re = 35. The least-square fitting indicates that both λ_{max} and λ_{min} exhibit excellent power-law relationships with r. It is seen that according to λ_{max} and λ_{min}, the parameter space (r, λ) can be clearly divided into three regimes, that is, the small particle leaving the large particle behind ($\lambda > \lambda_{max}$), the large particle leaving the small particle behind ($\lambda < \lambda_{min}$), and the

particles interacting with each other ($\lambda_{min} \leqslant \lambda \leqslant \lambda_{max}$). Note that the range between λ_{min} and λ_{max} narrows as r increases. It is also seen that both λ_{max} and λ_{min} decrease quickly as r increases, indicating a smaller particle needs to be heavier to settle together with a large particle. A possible explanation for this behavior is provided as follows.

Due to the balance of gravity, buoyancy, and hydrodynamic forces, the averaged drag coefficients of the two particles can be formulated as follows:

$$\bar{C}_{D1} = \frac{\bar{F}_{D1}}{0.5\rho V_T^2 d_1} = \frac{\pi g d_1}{2V_T^2}(\gamma - 1), \tag{10a}$$

$$\bar{C}_{D2} = \frac{\bar{F}_{D2}}{0.5\rho V_T^2 d_2} = \frac{\pi g d_1}{2V_T^2}(\lambda\gamma - 1)r. \tag{10b}$$

If the particles are settling together in the channel, we may simply assume that they have similar drag coefficients. As a result, the following formulation is obtained:

$$\frac{\bar{C}_{D1}}{\bar{C}_{D2}} = \frac{\gamma - 1}{(\lambda\gamma - 1)r} \sim 1. \tag{11}$$

It can be inferred from Eq. (11) that for a fixed γ the density ratio (λ) monotonously decreases as the diameter ratio (r) increases, which is approximately consistent with Fig. 6. From a qualitative viewpoint, the small particle will attain a larger settling velocity at a larger r, which may leave the large particle behind. Therefore, a smaller λ is needed to slow down the small particle to make sure they settle together in the channel, which is responsible for a smaller λ_{max} at a larger r. Similarly, the large particle will not leave a small particle with increasing r behind when λ remains unchanged. The small particle should be light enough (i.e., small λ) to make sure that it cannot catch up with the large particle. This results in a smaller λ_{min} at a larger r.

The effects of the Reynolds number on λ_{min} and λ_{max} are depicted in Fig. 7. Apart from Re = 35, two other sets of Reynolds numbers, that is, Re = 10 and 50, are taken into account. It can be seen that the power-law relationship holds for all Reynolds numbers considered. For a fixed diameter ratio (r), the value of λ_{min} is smaller at a higher Reynolds number, which is true over the entire range of r considered here [Fig. 7(a)]. A similar behavior is visible for λ_{max} when $r < 0.5$ [Fig. 7(b)]. However, the primary mechanism is different. When a large particle takes the lead, the effects of the wake behind it become significant as Re increases, giving rise to a stronger hydrodynamic interaction at a higher Re. Therefore, a small particle with lower density can possibly be sucked into the wake of the large particle. This results in a smaller λ_{min} at a higher Re. On the other hand, when the small particle takes the lead, the wake behind it is narrow, which has insignificant effects on the motion of the large particle. It is known that the drag coefficient of a particle decreases with Re. Due to the wall effects, the settling velocity of the small particle increases faster than that of the large particle as Re increases. As a result, a small particle with lower density may leave the large particle behind when the Reynolds number is higher. This is responsible for a smaller λ_{max} at a higher Re. For large values of r ($r > 0.5$), the wall effects on the small particle are significant as well. Therefore, the effects of Re on λ_{max} become negligible [Fig. 7(b)].
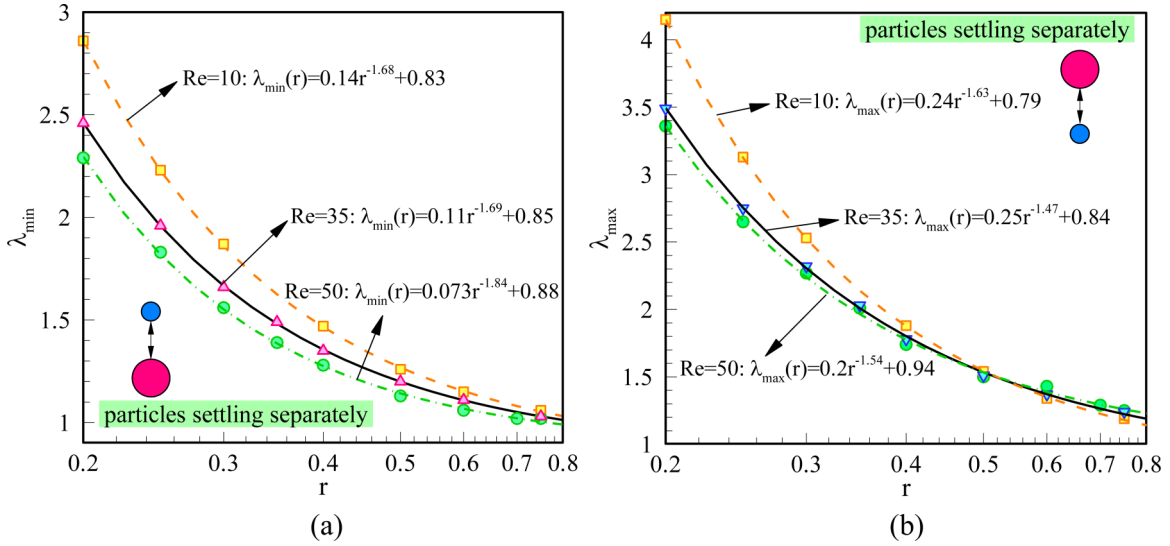
FIG. 7. Effects of the Reynolds number on (a) $\lambda_{min}(r)$ and (b) $\lambda_{max}(r)$, respectively.

Figure 8 summarizes the patterns of particle motion for the present system for $0.2 \leqslant r \leqslant 0.4$ at four representative Reynolds numbers (i.e., Re = 30, 35, 40, and 50). Note that for each Re, the least-square fittings for both $\lambda_{min}(r)$ and $\lambda_{max}(r)$ are indicated. According to both values of λ and r, three types of particle pattern are identified, i.e., DKT, VSS (vertical steady state), and HOM. Note that the DKT-I and DKT-II are used here to denote two kinds of DKT motion, as shown in Figs. 9(a) and 9(b), respectively. The most significant difference between them is that a process of "inverse drafting" occurs for the DKT-II [Fig. 9(b)]. After the tumbling, the small particle will quickly move to a position directly below the large one when it is heavy enough (i.e., large λ). As a consequence, the large particle is now located at the wake of the small one and begins to settle with increasing velocity, leading to the process of inverse drafting. This inverse drafting has a significant influence on the settling velocity of the particles, which will be discussed in the next section. Moreover, the relative particle trajectories resulting from another two initial positions of the small particle are also shown in Fig. 9 for each case, which are clearly seen to converge to its corresponding pattern when the initial transients are passed. From Figs. 4 and 9 we may conclude that all these patterns (i.e., DKT, HOM, and VSS) are the attractors of the present dynamical system (Fig. 2).

It is evident from Fig. 8 that the pattern of HOM occurs only for $r \sim 0.3$ at Re $\geqslant$ 35. In addition, Fig. 8 reveals a vertical steady state (VSS) for $r < 0.4$ when the density ratio between particles (λ) is close to λ_{max}. Figure 10 shows the corresponding instantaneous flow fields for both patterns. The pattern of VSS, with the large particle directly above the small particle, is somewhat unique because it forms a stable in-line structure at such a close distance [Fig. 10(a)]. This could not be possible for two identical particles because of the effects of the wake. In fact, the pattern of VSS is only seen at small values of r, which is similar to the HOM (Fig. 8). For large r, the effects of the wake behind the small particle are getting strong. The large particle may accelerate and comes close to the small one. Therefore, neither HOM nor VSS occurs

for $r \geqslant 0.4$. In particular, Fig. 8 indicates that upon increasing λ, the HOM may bifurcate into the VSS at low Re or small r.

B. Features of the HOM pattern

Figure 11 presents the relative particle trajectories as a function of the density ratio of particles (λ) for $r = 0.3$ at Re = 40 and 50. Note that for each λ, the relative particle trajectory, that is, the limit cycle constructed by ΔX^* and ΔY^*, is shaped like a lemniscate curve with symmetry with respect to the center line ($\Delta X^* = 0$) in most cases where both particles oscillate symmetrically about the channel axis (i.e., $\lambda \geqslant 2.17$ at Re = 40 and $\lambda \geqslant 2.12$ at Re = 50). This behavior is quite different from the periodic motion of particles with different densities but the same size [19] in terms of both the shape and size of the relative particle trajectory. Figure 11 also suggests that the particles oscillate in both vertical and horizontal directions. However, the size of the limit cycle indicates that the amplitude of horizontal oscillations is much larger (at least ten times) than that of vertical oscillations. In other words, horizontal oscillation dominates the motion of the two particles. Therefore, it is appropriate to refer to this behavior as the pattern of horizontal oscillatory motion (HOM).

As illustrated in Fig. 11, for each Re, the relative particle trajectory is seen to shift downward as λ increases, with decreasing size of the limit cycle except for small values of λ. This can be explained as follows. For a larger λ, the small particle is heavier and moves farther away from the large particle. As a result, the hydrodynamic interaction between them becomes weaker, leading to a smaller amplitude of oscillations. Upon further increasing λ, the particles may reach a steady state (VSS) instead of oscillating at low Re or small r, as indicated by Fig. 8, which is in accordance with the observation made in Fig. 11.

The phase diagrams constructed by X_1^* and X_2^* are presented in Fig. 12 for the same Reynolds numbers as in Fig. 11. Also shown in Fig. 12 is the Strouhal number (St = $f d_1/U_0$,
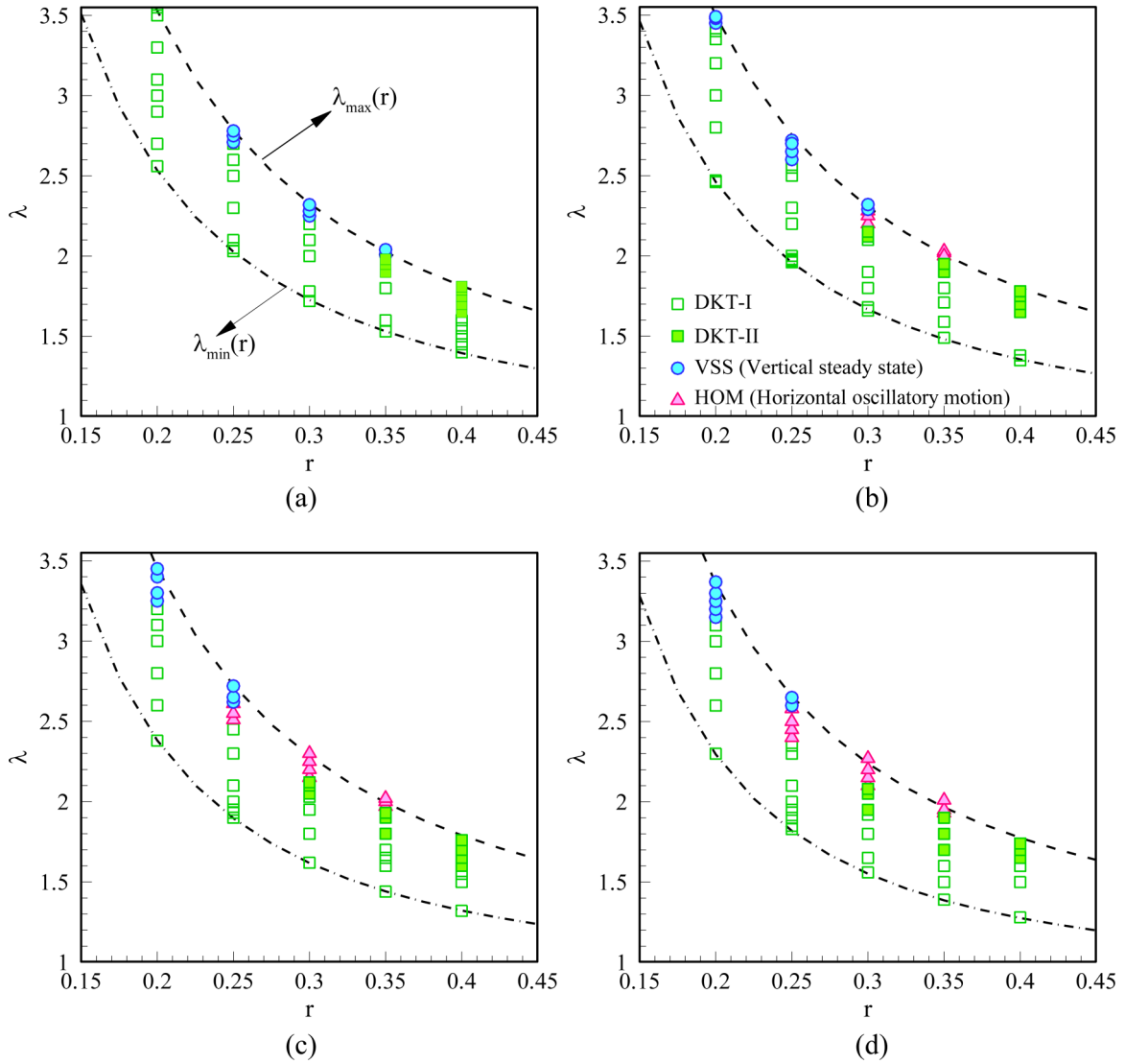
FIG. 8. Phase diagram for the parameter space (r, λ) at different Reynolds numbers: (a) Re = 30, (b) Re = 35, (c) Re = 40, and (d) Re = 50. Three types of particle motion are identified: DKT (drafting, kissing, and tumbling), VSS (vertical steady state), and HOM (horizontal oscillatory motion).

where f is the frequency of particle oscillations) for each λ. It can be seen that for each λ, the amplitude of X_1^* is larger than that of X_2^*, reflecting the fact that the large particle always oscillates more strongly. This tendency becomes more noticeable as λ increases. For instance, the amplitude of X_1^* is nearly 20% larger than that of X_2^* for $\lambda = 2.12$ at Re = 50. This value becomes nearly 90% for $\lambda = 2.17$ at the same Re, as shown in Fig. 12(b). In particular, for both Reynolds numbers, the oscillations of the two particles become nearly out of phase at large values of λ, suggesting that the large particle moves to its rightmost position when the small one moves to its leftmost position and vise versa. In comparison with the amplitude of oscillations, the Strouhal number shows an opposite trend upon increasing λ.

As is known, the particles settling in a narrow channel may interact with each other as well as with the channel walls. To illustrate this the minimum distances between each particle and walls (D_{W1}^* and D_{W2}^*) at different density ratios (λ) are compared with those between the particles (D_P^*) in

Fig. 13. According to Fig. 11, as λ increases the particles are getting further apart from one another, resulting in a larger D_P^* at a larger λ. Similarly, both D_{W1}^* and D_{W2}^* are seen to monotonously increase with λ for both Reynolds numbers shown in Fig. 13. Furthermore, it is shown that for a fixed λ the large particle always moves closer to the walls ($D_{W1}^* < D_{W2}^*$) when both particles oscillate symmetrically with respect to the channel axis (i.e., $\lambda \geqslant 2.17$ at Re = 40 and $\lambda \geqslant 2.12$ at Re = 50). More importantly, it is seen that either one of D_{W1}^* and D_{W2}^* is considerably larger than D_P^* irrespective of λ, suggesting that for the pattern of HOM the hydrodynamic interaction between the particles is stronger as compared with that between the particles and walls.

To further shed light on the pattern of HOM, the maximum horizontal velocity of the large particle ($|U_1^*|_M$) as a function of λ is shown in Fig. 14 for Re = 35, 40, and 50. The value of $|U_1^*|_M$ may be considered evidence of the intensity of particle oscillations. As shown in Fig. 14, for each Re, the value of
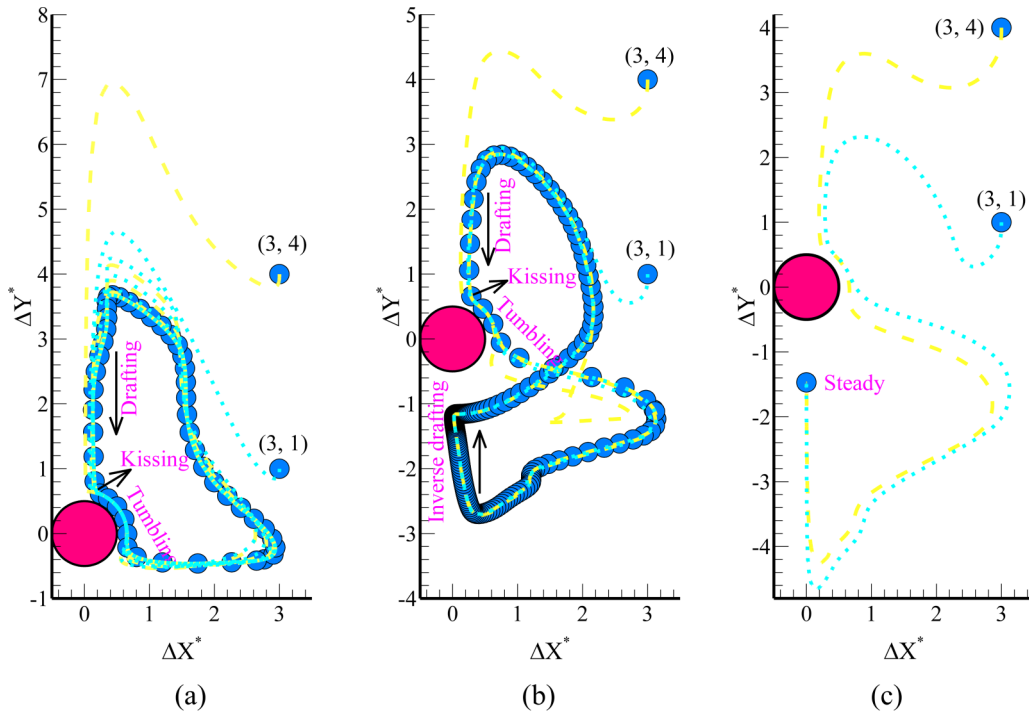
FIG. 9. Time-series snapshots of the relative motion of the particles showing different patterns for $r = 0.3$ at Re = 35: (a) DKT-I ($\lambda = 1.85$), (b) DKT-II ($\lambda = 2.15$), and (c) VSS ($\lambda = 2.3$). The snapshots are captured every 1000 time steps. Also shown are the relative particle trajectories resulting from another two initial positions of the small particle for each pattern.

$|U_1^*|_M$ seems to decrease linearly as λ increases except for small λ, which is consistent with Fig. 11. It is known that a single particle settling in a fluid may oscillate horizontally owing to the occurrence of vortex shedding when the Reynolds number is high enough. To provide a comparison, additional simulations were conducted for the settling of the large particle alone in the same channel at much higher Reynolds numbers (i.e., Re = 100, 120, and 150). The corresponding

results are compared with those obtained from the HOM in Fig. 14. It is clearly seen that the large particle gains a larger oscillatory velocity for almost all cases of the HOM. The hydrodynamic interaction induced by a small particle gives rise to the strong oscillations of the large particle.

It can be seen from Fig. 8 that for a fixed diameter ratio (r), the particles can exhibit different patterns of motion as λ increases from $\lambda_{\min}$ to $\lambda_{\max}$. To illustrate this, the terminal
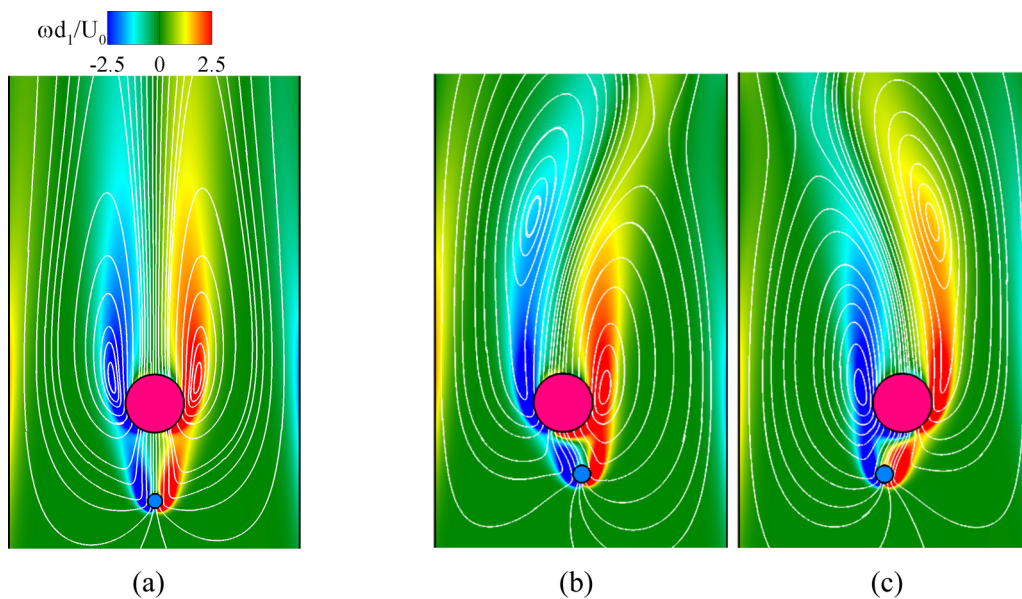
FIG. 10. Flow features for the patterns of (a) VSS ($r = 0.25$ and $\lambda = 2.65$) and (b,c) HOM ($r = 0.3$ and $\lambda = 2.12$) at Re = 50. For the pattern of HOM, that is, (b,c), the results are chosen at the times when the large particle reaches its leftmost and rightmost positions, respectively.
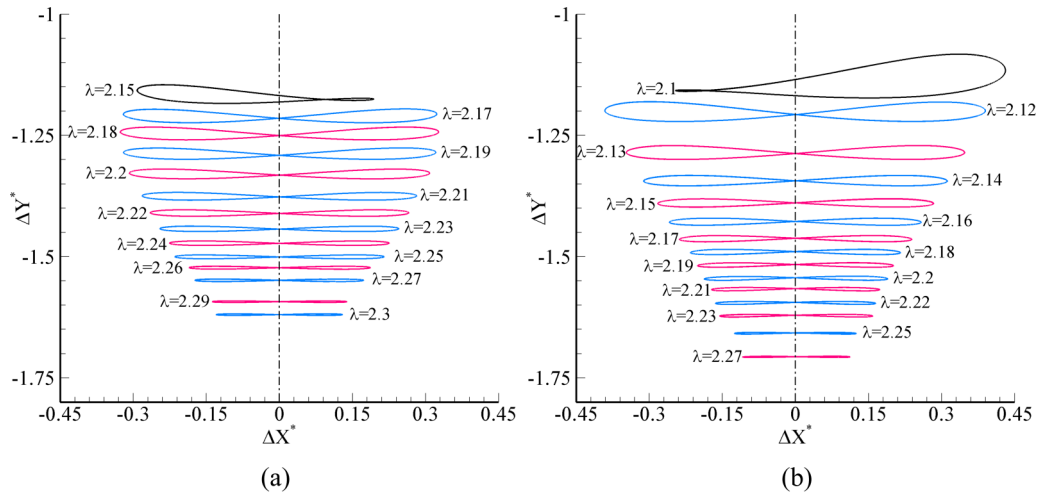
FIG. 11. Limit cycles constructed by ΔX^* and ΔY^* (i.e., the relative particle trajectories) as a function of λ for $r = 0.3$ at (a) Re = 40 and (b) Re = 50, respectively.
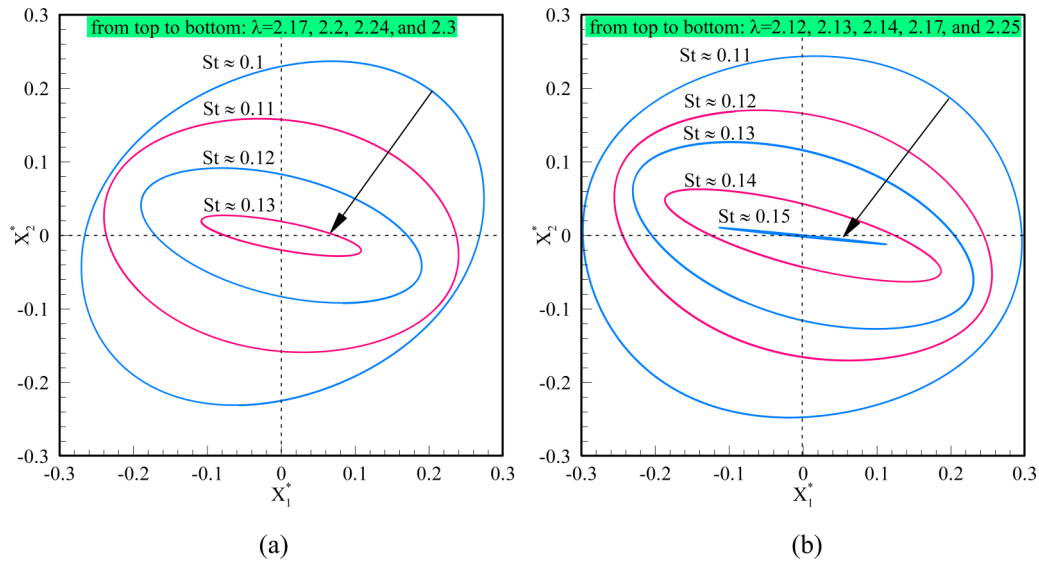
FIG. 12. Limit cycles constructed by X_1^* and X_2^* as a function of λ for $r = 0.3$ at (a) Re = 40 and (b) Re = 50, respectively. Also shown in the figure is the Strouhal number (St $= f d_1/U_0$, where f is the frequency of oscillations) for each λ.
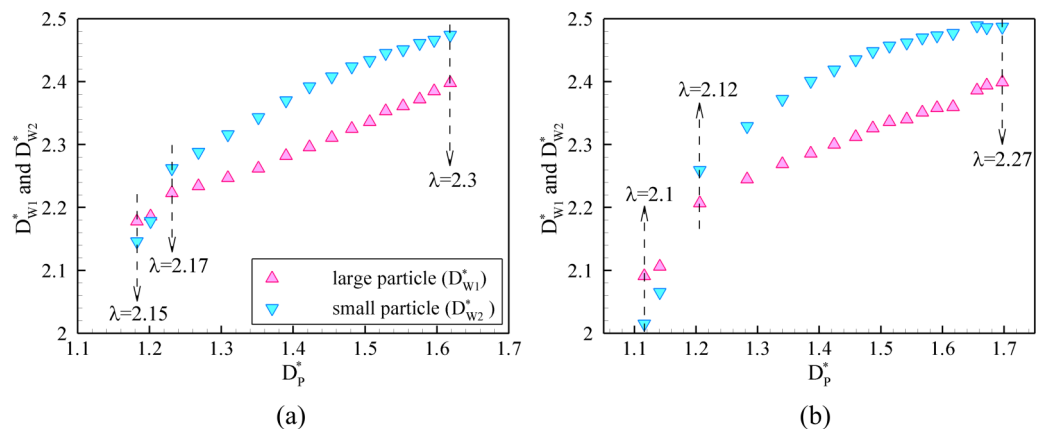
FIG. 13. Minimum distances between each of the particles and walls (D_{W1}^* and D_{W2}^*) at different λ vs minimum distances between the particles (D_P^*) for (a) Re = 40 and (b) Re = 50, respectively.
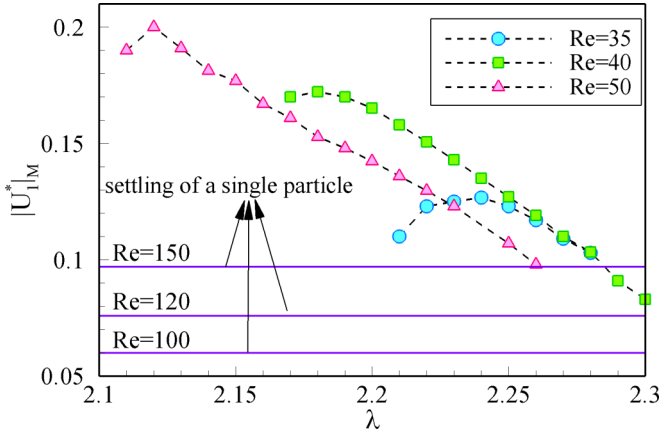
FIG. 14. Maximum horizontal velocities of the large particle ($|U_1^*|_M$) as a function of λ for $r = 0.3$ at different Reynolds numbers. The corresponding results for the settling of a single particle (i.e., the large particle alone) at Re = 100, 120, and 150 are also indicated to provide a comparison.

settling velocity of the particles ($|V_T^*|$) as a function of λ for $r = 0.3$ is shown in Fig. 15 for Re = 35, 40, and 50. Note that $|V_T^*|$ is averaged over time when the particles reach a statistically stationary state. As shown in Fig. 15, the entire sequence of transitions is clearly seen. Three regions can be identified according to the value of λ: DKT-I, DKT-II, and HOM. In comparison with the DKT-I, the inverse drafting induces a sudden increase in the settling velocity of the particles for the DKT-II (see also Fig. 9). The primary reason is that the particles experience a smaller drag when they form an in-line structure along the direction of gravity. More importantly, upon increasing λ, the DKT-II may bifurcate into another pattern of particle motion (i.e., the HOM), along with a second sudden increase in the settling velocity (Fig. 15). The reason for this is the same as above. Similar to Fig. 14, the settling of a single particle (i.e., the large particle alone) was also considered to provide a comparison, for which the values of $|V_T^*|$ at the same Reynolds numbers (i.e., Re = 35, 40, and
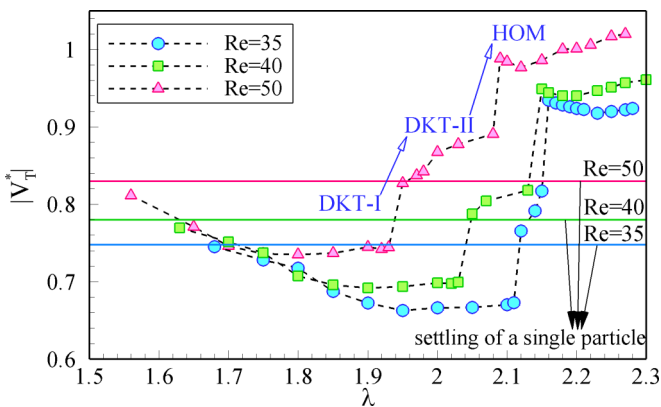
FIG. 15. Terminal settling velocities of the particles ($|V_T^*|$) as a function of λ for $r = 0.3$ at different Reynolds numbers showing the entire sequence of transitions (i.e., DKT-I → DKT-II → HOM). Also shown in the figure are the corresponding results of a single particle (i.e., the large particle alone) at the same Reynolds numbers.
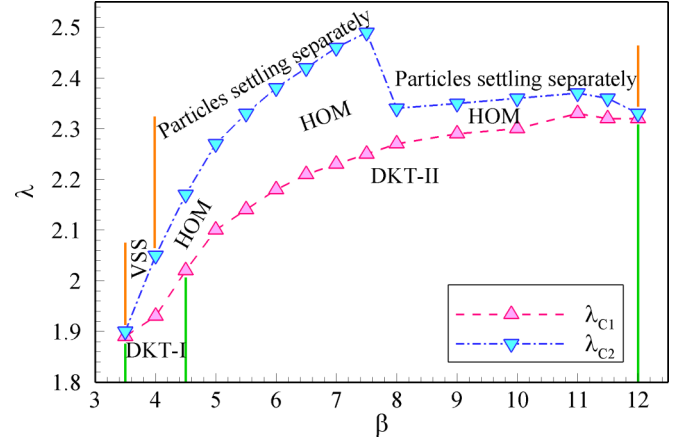
FIG. 16. λ ranges ($\lambda_{C1} \leqslant \lambda \leqslant \lambda_{C2}$) for the occurrence of HOM at different confinement ratios ($\beta = 3.5$–12).

50) are indicated in Fig. 15. It is interesting to note that the following relationship holds for every Re considered: $|V_T^*|_{HOM} > |V_T^*|_{DKT-II} > |V_T^*|_{Single} > |V_T^*|_{DKT-I}$. Note that $|V_T^*|_{Single}$ refers to the case of a single particle. The pattern of HOM, with the large particle directly over the small particle, results in a settling velocity that is more than 20% larger than that of a single particle.

C. Effects of the confinement ratio

The pattern of HOM is clearly a combined effect of the hydrodynamic interaction between particles and the particle-wall interaction. The wall effects may be crucial to the pattern of HOM, which were examined by varying the confinement ratio (β) in this work. For simplicity, the Reynolds number and the diameter ratio are fixed; that is, Re = 50 and $r = 0.3$. The phase diagram for the parameter space (β, λ) is presented in Fig. 16.

It is found that the pattern of HOM exists for a wide range of β, that is $\beta = 3.5$–12, as shown in Fig. 16. For narrow channels (i.e., $\beta \leqslant 4.5$), the transition from DKT-I to HOM is observed at $\lambda = \lambda_{C1}$, which differs from that for wide channels (see also Fig. 15). In addition, for $\beta > 4$, the particles settle separately in the channel at $\lambda > \lambda_{C2}$, indicating that
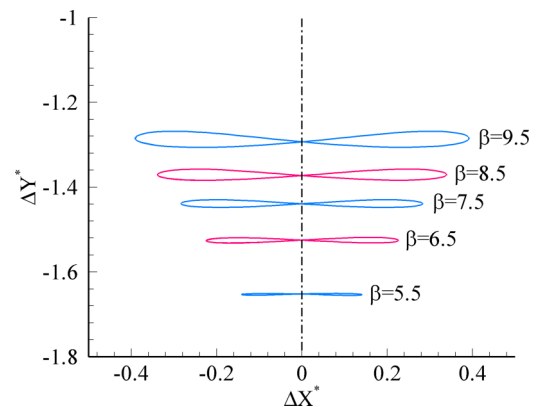
FIG. 17. Relative particle trajectories (i.e., the limit cycles constructed by ΔX^* and ΔY^*) at different confinement ratios ($\beta = 5.5$–9.5) for $\lambda = 2.3$.
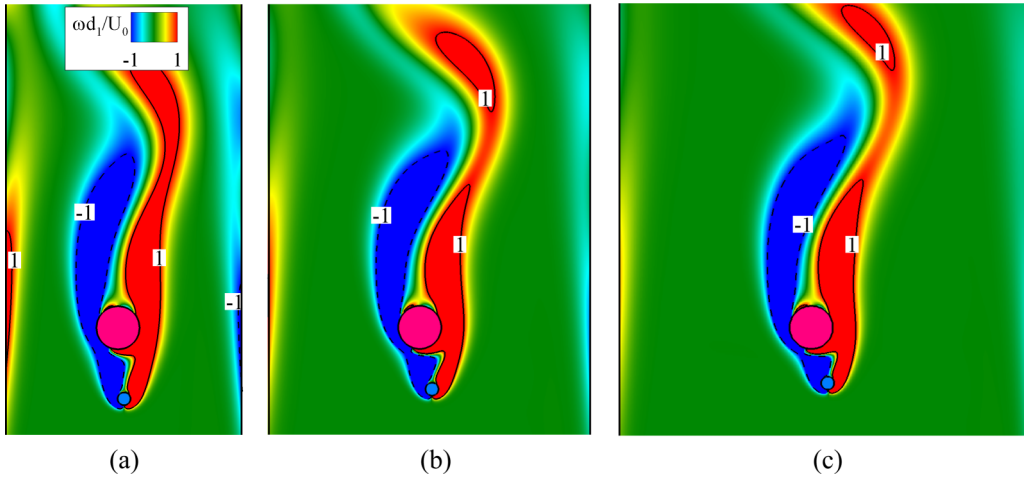
FIG. 18. Instantaneous vorticity contours for $\lambda = 2.3$ at different confinement ratios: (a) $\beta = 5.5$, (b) $\beta = 7.5$, and (c) $\beta = 9.5$. All results are chosen when the large particle reaches its leftmost position.

$\lambda_{C2} = \lambda_{max}$. By contrast, a Hopf bifurcation occurs at $\lambda = \lambda_{C2}$ for $\beta \leqslant 4$, leading to the pattern of VSS at $\lambda > \lambda_{C2}$.

An increasing λ range for the HOM is seen as the confinement ratio increases when $\beta \leqslant 7.5$. However, the opposite trend is observed for $\beta > 7.5$. In particular, Fig. 16 shows an abrupt decrease in the λ range at a critical confinement ratio ($\beta \approx 7.5$), suggesting that the particles may interact with each other in a different manner for $\beta > 7.5$. To gain insights into this issue, the relative particle trajectories as well as the instantaneous vorticity contours for $\beta = 5.5$–9.5 are shown in Figs. 17 and 18, respectively. The density ratio between particles was chosen as $\lambda = 2.3$. The size of the limit cycle monotonously increases with β (Fig. 17), suggesting that the particles oscillate more strongly in a wider channel because of the decreasing wall effects. Both Figs. 17 and 18 reflect the fact that the small particle gets closer to the large one at a larger β. However, it appears that no sudden change occurs in the relative particle trajectory of the particles when the confinement ratio β varies from 5.5 to 9.5 (Fig. 17).

The situation becomes different for the terminal velocity ($|V_T^*|$) and the period of particle oscillations (T^*), as shown in Fig. 19. The same density ratio as Fig. 17 was chosen. It seems that the value of $|V_T^*|$ increases linearly as β increases [Fig. 19(a)]. This is reasonable because the wall effects become weaker in a wider channel (see also Fig. 18). In particular, a sudden change in $|V_T^*|$ is visible at $\beta \approx 7.5$, leading to very different slopes for $\beta < 7.5$ (slope ≈ 0.027) and $\beta > 7.5$ (slope ≈ 0.014), respectively. This suggests that the terminal velocity of the particles increases at a much lower speed in wide channels (i.e., $\beta > 7.5$). The sudden change in $|V_T^*|$ is consistent with that seen in Fig. 16. Similar behavior is observed for the period of particle oscillations [Fig. 19(b)] except that a larger slope (slope ≈ 0.455) was obtained for $\beta > 7.5$ than that (slope ≈ 0.294) for $\beta < 7.5$, suggesting that the frequency of particle oscillations decreases at a higher speed when $\beta > 7.5$. This is responsible for the sudden change in the terminal velocity of the particles [Fig. 19(a)]. It is known that the particles may acquire a larger settling velocity if they stay close to the channel axis owing to a smaller drag. The
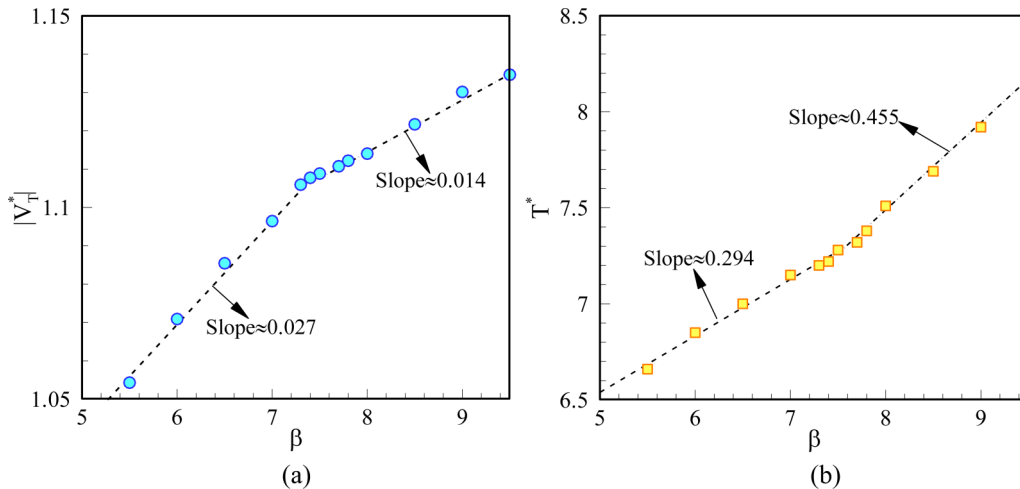
FIG. 19. Linear relationships of (a) the terminal velocity of particles and (b) the period of particle oscillations with the confinement ratio for $\lambda = 2.3$.
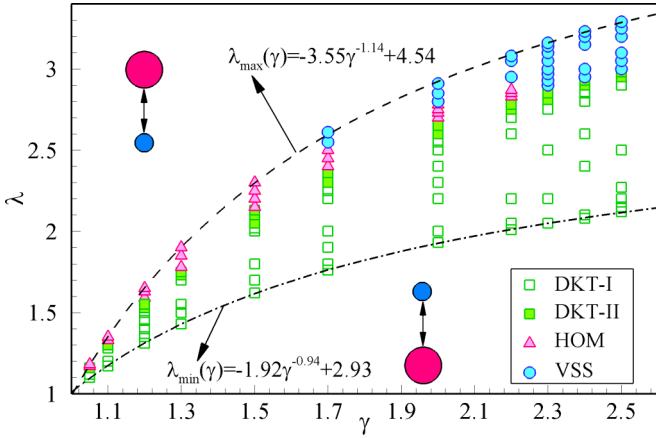
FIG. 20. Phase diagram for the particles in the parameter space (γ, λ) at Re = 40. For small $\gamma(\gamma \leqslant 1.5)$, the sequence of "DKT-I $\rightarrow$ DKT-II $\rightarrow$ HOM" is seen. For intermediate $\gamma(1.7 \leqslant \gamma \leqslant 2.2)$, the sequence of "DKT-I $\rightarrow$ DKT-II $\rightarrow$ HOM $\rightarrow$ VSS" is seen. For large $\gamma(\gamma \geqslant 2.3)$, the pattern of HOM cannot be seen.

larger the value of T^*, the more time the particles stay away from the channel axis.

D. Effects of the particle-to-fluid density ratio

This section examines the effects of the density ratio between the large particle and fluid (i.e., $\gamma = \rho_1/\rho$). As is known, the value of γ represents the inertia of the particles, which deserves much attention as well in this study. For simplicity, the Reynolds number and the diameter ratio are fixed; that is, Re = 40 and $r = 0.3$. In addition, the computations were performed in a 5 d_1 channel. The phase diagram for the parameter space (γ, λ) is presented in Fig. 20 for the range of γ between 1.05 and 2.5$(1.05 \leqslant \gamma \leqslant 2.5)$.

The effects of the particle-fluid density ratio (γ) on the particle motion are significant, as shown in Fig. 20. For small $\gamma(\gamma \leqslant 1.5)$, the sequence of transitions (i.e., DKT-I $\rightarrow$ DKT-II $\rightarrow$ HOM) is seen as λ varies from $\lambda_{\min}$ to $\lambda_{\max}$. For

intermediate $\gamma(1.7 \leqslant \gamma \leqslant 2.2)$, the pattern of HOM bifurcates into the VSS when λ is close to $\lambda_{\max}$. However, the transition from the DKT-II to VSS is seen for large $\gamma(\gamma \geqslant 2.3)$ through a Hopf bifurcation. Therefore, the pattern of HOM does not occur for $\gamma \geqslant 2.3$. This is reasonable because the inertia of the particles becomes so strong at large γ that the oscillations are ceased. In other words, the wake cannot induce the oscillatory motion of particles that are too heavy.

In particular, either one of $\lambda_{\max}$ and $\lambda_{\min}$ exhibits an excellent power-law relationship with the particle-fluid density ratio γ, which is similar to Fig. 6. It is also interesting to find that both $\lambda_{\max}$ and $\lambda_{\min}$ approach 1 at $\gamma = 1$, which corresponds to the case of neutrally buoyant particles. A significant difference between Figs. 6 and 20 is that either one of $\lambda_{\max}$ and $\lambda_{\min}$ increases as γ increases. For this a possible explanation is provided as follows. From Eq. (11) the following formulation is easily obtained:

$$r \sim \frac{\gamma - 1}{\lambda\gamma - 1}. \tag{12a}$$

As a reminder, r and λ denote the diameter and density ratios between the particles, respectively; i.e., $r = d_2/d_1$ and $\lambda = \rho_2/\rho_1$. Then, the relationship between λ and γ can be achieved:

$$\lambda \sim \frac{1}{r}\left(1 - \frac{1 - r}{\gamma}\right). \tag{12b}$$

Note that $r < 1$ holds for all cases studied. According to Eq. (12b), the value of λ monotonously increases as γ increases when the diameter ratio r is fixed. This is in accord with the observation made in Fig. 20.

Figures 21(a) and 21(b) present the relative particle trajectories at different λ for $\gamma = 1.2$ and $\gamma = 2$, respectively. It is seen that the size of the limit cycle is much larger for $\gamma = 1.2$ [Fig. 21(a)], indicating that the particles are oscillating more strongly at small particle inertia. Moreover, it is clearly shown that the small particle gets much closer to the large one for $\gamma = 2$ when they are settling in the channel [Fig. 21(b)]. The reason is similar to the one mentioned above. The wake may
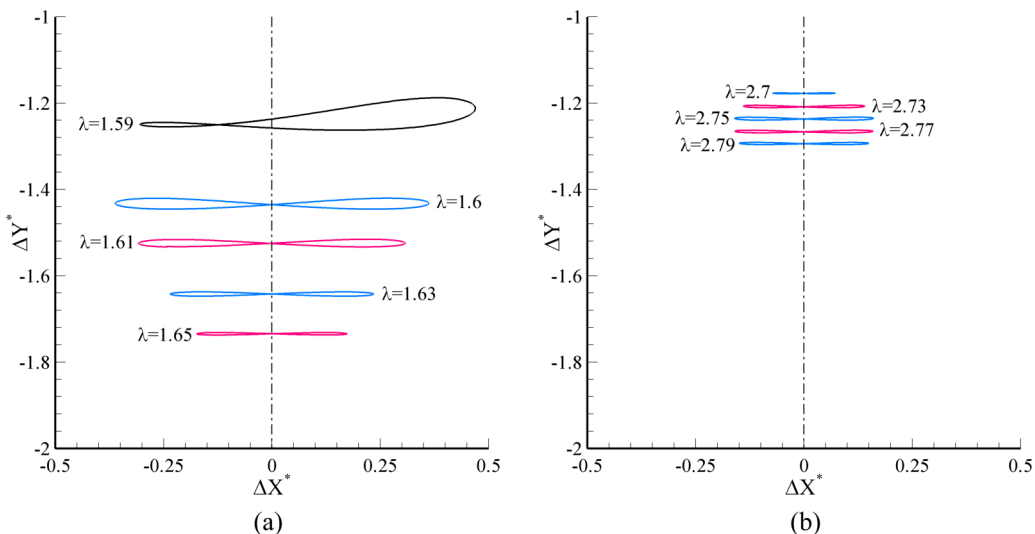
FIG. 21. Relative particle trajectories as a function of λ for (a) $\gamma = 1.2$ and (b) $\gamma = 2$, respectively, at Re = 40.

induce the oscillations of heavy particles that are at small distances.

VI. CONCLUSION

The settling of two unequal particles under gravity in a two-dimensional channel was numerically studied using the lattice Boltzmann method. Both the density ratio (i.e., $\lambda = \rho_2/\rho_1$) and diameter ratio (i.e., $r = d_2/d_1$) between particles were taken into account. Much attention was paid to a pattern of horizontal oscillatory motion (HOM) resulting from the interaction between the two unequal particles at intermediate Reynolds numbers. The concluding remarks are as follows:

(1) For a fixed r, there exists a range of $\lambda(\lambda_{\min} \leqslant \lambda \leqslant \lambda_{\max})$ within which the particles interact with each other all the time in the channel. This study shows that both $\lambda_{\min}$ and $\lambda_{\max}$ decrease with r following excellent power-law relationships over the entire range of Reynolds numbers considered ($10 \leqslant$ Re $\leqslant 50$).

(2) The pattern of HOM occurs for $r \sim 0.3$ at Re $\geqslant$ 35, which is characterized by a structure with a large (but light) particle directly above a small (but heavy) particle and strong oscillations of both particles in the horizontal direction. The terminal velocity of the particles illustrates the sequence of transitions of particle motion over the range of $[\lambda_{\min}, \lambda_{\max}]$; that is, DKT-I $\rightarrow$ DKT-II $\rightarrow$ HOM. Note that DKT-I and DKT-II represent two kinds of "drafting, kissing, and

tumbling" motion. In particular, each transition is accompanied by an abrupt increase in the terminal velocity. The results also indicate that upon increasing λ, the HOM may bifurcate into a vertical steady state (VSS) at low Re or small r.

(3) The HOM pattern exists for a wide range of confinement ratios (e.g., $3.5 \leqslant \beta \leqslant 12$ at Re $= 50$). For narrow channels, the transition from the DKT-I to HOM is observed, which differs from that for wide channels (DKT-I $\rightarrow$ DKT-II $\rightarrow$ HOM). In particular, there is a sudden decrease in the λ range for the occurrence of HOM at a critical β, beyond which the particles interact differently in terms of the decreasing slope of the terminal particle velocity and the increasing slope of the period of oscillations.

(4) The effects of the particle-to-fluid density ratio (i.e., $\gamma = \rho_1/\rho$) were also examined. Either one of $\lambda_{\min}$ and $\lambda_{\max}$ increases with γ obeying an excellent power-law relationship. For small γ (e.g., $\gamma \leqslant 1.5$ at Re $= 40$), the sequence of transitions (i.e., DKT-I $\rightarrow$ DKT-II $\rightarrow$ HOM) is seen. For intermediate γ, the HOM bifurcates into the VSS eventually. However, the pattern of HOM may not take place at large γ due to strong particle inertia.

[1] A. F. Fortes, D. D. Joseph, and T. S. Lundgren, J. Fluid Mech. **177**, 467 (1987).

[2] W. B. Daniel, R. E. Ecke, G. Subramanian, and D. L. Koch, J. Fluid Mech. **625**, 371 (2009).

[3] S. M. Dash and T. S. Lee, Comput. Fluids **123**, 218 (2015).

[4] H. H. Hu, D. D. Joseph, and M. J. Crochet, Theor. Comput. Fluid Dyn. **3**, 285 (1992).

[5] J. Feng, H. H. Hu, and D. D. Joseph, J. Fluid Mech. **261**, 95 (1994).

[6] D. M. Nie, J. Z. Lin, and M. J. Zheng, Commun. Comput. Phys. **16**, 675 (2014).

[7] L. Wang, Z. L. Guo, and J. C. Mi, Comput. Fluids **96**, 20 (2014).

[8] C. K. Aidun and E. J. Ding, Phys. Fluids **15**, 1612 (2003).

[9] R. Verjus, S. Guillou, A. Ezersky, and J.-R. Angilella, Phys. Fluids **28**, 123303 (2016).

[10] Y. Zhang, Y. H. Zhang, G. Pan, and S. Haeri, J. Comput. Phys. **368**, 1 (2018).

[11] F. Charru, E. Larrieu, J. B. Dupont, and R. Zenit, J. Fluid Mech. **570**, 431 (2007).

[12] H. Lee and S. Balachandar, Int. J. Multiphase Flow **88**, 116 (2017).

[13] L. H. Tsai, C. C. Chang, T.-W. Pan, and R. Glowinski, Int. J. Comput. Fluid Dyn. **32**, 158 (2018).

[14] T.-W. Pan and R. Glowinski, Phys. Rev. E **96**, 063103 (2017).

[15] X. T. Zhang, H. H. Liu, Y. Zhang, and L. Wang, Phys. Rev. Fluids **5**, 014304 (2020).

[16] S. G. Huisman, T. Barois, M. Bourgoin, A. Chouippe, T. Doychev, P. Huck, C. E. Bello Morales, M. Uhlmann, and R. Volk, Phys. Rev. Fluids **1**, 074204 (2016).

[17] W. Fornari, M. Ardekani, and L. Brandt, J. Fluid Mech. **848**, 696 (2017).

[18] D. M. Nie, J. Z. Lin, and Q. Gao, Comput. Fluids **156**, 353 (2017).

[19] D. M. Nie and J. Z. Lin, Phys. Rev. E **99**, 053112 (2019).

[20] D. M. Nie and J. Z. Lin, J. Fluid Mech. **896**, A12 (2020).

[21] Y. H. Qian, D. D'Humières, and P. Lallemand, Europhys. Lett. **17**, 479 (1992).

[22] P. Lallemand and L. S. Luo, J. Comput. Phys. **184**, 406 (2003).

[23] R. Mei, D. Yu, W. Shyy, and L.-S. Luo, Phys. Rev. E **65**, 041203 (2002).

[24] C. K. Aidun, Y. Lu, and E. J. Ding, J. Fluid Mech. **373**, 287 (1998).

[25] X. Yuan and R. Ball, J. Chem. Phys. **101**, 9016 (1994).

[26] D. Wan and S. Turek, Int. J. Numer. Methods Fluids **51**, 531 (2006).

[27] R. Glowinski, T. W. Pan, T. I. Hesla, D. D. Joseph, and J. Périaux, J. Comput. Phys. **169**, 363 (2001).